Atmospheric
Measurement
Techniques
Discussions

Open Access

Accurate mobile remote sensing of XCO$_2$ and XCH$_4$ latitudinal transects from aboard a research vessel

F. Klappenbach[1], M. Bertleff[1], J. Kostinek[1], F. Hase[1], T. Blumenstock[1], A. Agusti-Panareda[2], M. Razinger[2], and A. Butz[1]

[1]IMK-ASF, Karlsruhe Institute of Technology (KIT), Hermann-von-Helmholtz-Platz 1, 76344 Eggenstein-Leopoldshafen, Germany
[2]The European Centre for Medium-Range Weather Forecasts (ECMWF), Shinfield Park, Reading, RG2 9AX, UK

Correspondence to: F. Klappenbach (friedrich.klappenbach@kit.edu)

Discussion Paper | Discussion Paper | Discussion Paper | Discussion Paper

AMTD

8, 7413–7453, 2015

Accurate mobile remote sensing of XCO$_2$ and XCH$_4$

F. Klappenbach et al.

Title Page

Abstract	Introduction
Conclusions	References
Tables	Figures

◄ | ►

◄ | ►

Back | Close

Full Screen / Esc

Printer-friendly Version

Interactive Discussion

Abstract

A portable Fourier Transform Spectrometer (FTS), model EM27/SUN, is deployed on-board the research vessel *Polarstern* to measure the column-average dry air mole fractions of carbon dioxide (XCO$_2$) and methane (XCH$_4$) by means of direct sunlight absorption spectrometry. We report on technical developments as well as data calibration and reduction measures required to achieve the targeted accuracy of fractions of a percent in retrieved XCO$_2$ and XCH$_4$ while operating the instrument under field conditions onboard the moving platform during a six week cruise through the Atlantic from Cape Town (South Africa, $34°$ S, $18°$ E) to Bremerhaven (Germany, $54°$ N, $19°$ E). We demonstrate that our solar tracker typically achieves a tracking precision of better than $0.05°$ toward the center of the sun throughout the ship cruise which facilitates accurate XCO$_2$ and XCH$_4$ retrievals even under harsh ambient wind conditions. We define several quality filters that screen spectra e.g. when the field-of-view is partially obstructed by ship structures or when the lines-of-sight cross the ship exhaust plume. The measurements in clean oceanic air, can be used to characterize a spurious air-mass dependency. After the campaign, deployment of the spectrometer side-by-side the TCCON (Total Carbon Column Observing Network) instrument at Karlsruhe, Germany, allows for determining a calibration factor that makes the entire campaign record traceable to World Meteorological Organization (WMO) standards. Comparisons to observations of the GOSAT satellite and concentration fields modeled by the European Centre for Medium-Range Weather Forecasts (ECMWF) within the project Monitoring of Atmospheric Composition and Climate – Interim Implementation (MACC-II) demonstrate that the observational setup is well suited to provide validation opportunities above the ocean and along interhemispheric transects.

1   Introduction

Carbon dioxide (CO$_2$) and methane (CH$_4$) are the most important anthropogenic greenhouse gases (Stocker et al., 2013). To understand their emission and uptake processes at the Earth's surface, inverse modeling approaches exploit the observed variability of the atmospheric concentration fields (e.g. Chevallier et al., 2010; Peylin et al., 2013). Estimating surface fluxes of CO$_2$ and CH$_4$ in particular requires accurate and spatially and temporally dense observations of the atmospheric abundances. Such observations have been delivered for decades by ground-based in-situ monitoring stations (e.g. Masarie et al., 2014) though their coverage in remote regions is sparse. Remote sensing of column-average CO$_2$ (XCO$_2$) and CH$_4$ (XCH$_4$) from satellites is an emerging technique that promises improved coverage and data density but faces challenging accuracy requirements on the order of fractions of a percent (e.g. Chevallier et al., 2007; Bergamaschi et al., 2009). Therefore, XCO$_2$ and XCH$_4$ soundings recorded by satellites such as Scanning Imaging Absorption Spectrometer for Atmospheric CHartographY (SCIAMACHY), Greenhouse Gases Observing Satellite (GOSAT) (Burrows et al., 1995; Bovensmann et al., 1999), or the recently launched Orbiting Carbon Observatory-2 (OCO-2) require thorough validation through ground-based measurements.

To this end, the Total Carbon Column Observing Network (TCCON) has been designed, currently operating more than 20 ground-based high-resolution lab Fourier Transform Spectrometers (FTS) at stations worldwide (Wunch et al., 2011; TCCON-Wiki, 2015). These ground-based FTS collect solar absorption spectra in direct-sun view allowing for accurate knowledge of the light path through the atmosphere and thereby, avoiding one of the largest sources of error for satellite remote sensing of XCO$_2$ and XCH$_4$ (Rayner and O'Brien, 2001). The typical accuracy of TCCON spectrometers is reported better than 0.8 ppm (parts per million) for XCO$_2$ and 7 ppb (parts per billion) for XCH$_4$ (Wunch et al., 2010). The TCCON FTS operate at high spectral resolution and therefore, require stationary containers that can house the rather bulky

and delicate instruments. Developments are ongoing to prove performance of smaller and more robust remote sensing instruments that can be easily deployed in remote regions, in larger numbers, and on mobile platforms (Kobayashi et al., 2010; Krings et al., 2011; Kawasaki et al., 2012; Petri et al., 2012; Gisi et al., 2012; Frey et al., 2015).

Here, we demonstrate performance of such a small and robust spectrometer for accurate observations of XCO_2 and XCH_4 on a mobile platform. We deploy an Bruker™ EM27/SUN FTS aboard the German research vessel (RV) *Polarstern* traveling from South Africa to Germany during a 5-week cruise in March/April 2014.

The EM27/SUN FTS is a table-top, portable instrument operating at medium spectral resolution of $0.5\,\mathrm{cm}^{-1}$. Performance of the EM27/SUN FTS in stationary configuration has been proven for XCO_2 by Gisi et al. (2012) using measurements side-by-side the TCCON instrument at Karlsruhe, Germany. Previously, Notholt et al. (1995) and Warneke et al. (2005) have shown that RV *Polarstern* is an excellent carrier to investigate hemispheric gradients of a large variety of atmospheric constituent including the man-made greenhouse gases. Instrumentation, however, is challenged by harsh ambient conditions. In particular, the moving platform poses a challenge for direct solar absorption spectroscopy since the solar intensity has to be fed precisely into the spectrometer´s entrance aperture, regardless the movements of the platform. In the view of satellite validation, shipborne measurements are particular interesting since currently there are only a few island observatories (e.g. Geibel et al., 2010; Schneider et al., 2012) that allow for validating XCO_2 and XCH_4 derived from glint-mode satellite operations over the oceans.

Figure 1 illustrates the track of RV *Polarstern* starting out at Cape Town, South Africa (34° S, 18° E) on 5 March 2014, and entering port at Bremerhaven, Germany, (54° N, 19° E) on 14 April 2014. During the cruise the EM27/SUN spectrometer operated whenever cloud conditions permitted direct-sun view on 31 out of 40 days, in total collecting 5693 spectra for which XCO_2 and XCH_4 can be derived. Beside recording solar absorption spectra, our housekeeping infrastructures monitored ambient pressure and temperature. Further, RV *Polarstern* is equipped with a meteorological station. In addi-

Accurate mobile remote sensing of XCO_2 and XCH_4

F. Klappenbach et al.

Title Page

Abstract | Introduction

Conclusions | References

Tables | Figures

◀ | ▶

◀ | ▶

Back | Close

Full Screen / Esc

Printer-friendly Version

Interactive Discussion

tion the the EM27/SUN, we operated a custom-built grating spectrometer. Design and performance of the latter will be reported in a forthcoming study.

Here, we first outline the instrument setup (Sect. 2) in particular focusing on a custom-built sun-tracker attached to the sun-viewing spectrometer. The sun-tracker must be able to compensates both, the relatively slow motion of the solar disk across the sky and the, occasionally, fast movements of the platform. Then, we detail data reduction measures to guarantee high accuracy and consistency of the XCO$_2$ and XCH$_4$ soundings throughout the ship cruise (Sect. 3). Finally, we illustrate the usefulness of the derived greenhouse gas concentrations for validation soundings from GOSAT and for evaluating the hemispheric concentration gradients in a global model (Sect. 4). Section 5 concludes the study.

2   Instrumentation

The key instrumentation consists of the EM27/SUN FTS (Sect. 2.2) available for purchase at Bruker™ Optics and a custom-built solar tracker (Sect. 2.1).

2.1   Custom-built solar tracking system

The solar tracker is based on the "Cam-tracker" setup initially designed for stationary platforms by Gisi et al. (2011). Here, it is modified for mobile applications and its performance is demonstrated through its operation on RV *Polarstern*. The system consists of two mirrors that rotate along an azimuth and elevation axis driven by two stepper motors and it is able to point toward every point on the sky hemisphere above the instrument. A camera observes the solar image centered about the entrance aperture of the spectrometer. An image analysis software fits circles to the solar image and the aperture. The mismatch between the circle centers drives a PID (proportional-integral-differential) control unit which adjusts the mirrors to finally recenter the solar image. On stationary platforms, PID control cycles exceeding a second are acceptable given that

the solar disk moves slowly across the sky. Under such conditions, Gisi et al. (2011) shows that tracking errors are typically less than 0.003° which is well below the targeted tracking accuracy of 0.05° needed to keep pointing-induced XCO_2 errors below 0.1 ppm.

Adapting the solar tracking system to mobile applications poses two major challenges:

– At start-up or after interruptions of the tracking operations, the solar tracker needs to find the solar disk without knowledge of the observatory's orientation. For stationary operations the attitude of the observatory is typically given at start-up (and left unchanged) and astronomical calculations provide the initial relative position of the sun.

– The PID control cycle needs to cope with the potentially fast motion of the platform in addition to the slow motion of the solar disk.

Basically, the tracking procedure can be split into two parts, that tackle the required adaptations: the coarse and the fine-tracking mode. The latter is a refinement of the concept proposed by Gisi et al. (2011). Both require additional or exchange of hardware.

The coarse-tracking mode relies on a 185° fish eye-lens (Lensation, BFM2320) mounted on a CMOS digital camera (VR-magic, model C-9+ PRO BW CMOS, 1288 × 1032 pixel) observing the sky hemisphere above the instrument. The approximate position of the solar disk is identified as the brightest spot on the camera image. A lookup-table generated through lamp calibration in our laboratory translates image positions into azimuth and elevation angles of the tracking mirrors. The angular resolution of the coarse-tracking is approximately $0.15° \, \text{pixel}^{-1}$ and strongly variable within the field of view. Thus, it is not accurate enough to perform the entire tracking process with the desired accuracy of 0.05°. But, the coarse-tracking ensures that the solar disc of about 0.53° diameter can be located within the Field-Of-View (FOV) of the fine-tracking camera, that is approximately 10–15°.

Once the solar image is within the FOV of the fine-tracking camera (VR-magic, model C-9+ PRO BW CMOS, 1288×1032 pixel, $f = 50\,\text{mm}$), coarse-tracking goes idle and fine-tracking mode takes over centering the solar image on the aperture of the spectrometer through a circle fitting routine. In order to enhance the tracking velocity for a moving platform, it is essential to update the motor control parameters (position, speed or acceleration) as frequently as possible. To minimize the time lost during communication between the fine-tracking camera and the control unit (Embedded PC-System, ARK by Advantech), the camera only transmits a region of interest of approximately $200\,\text{pixel} \times 200\,\text{pixel}$ out of the full camera frame of $1288\,\text{pixel} \times 1032\,\text{pixel}$ via USB. Additionally each motor connects via its own RS485 connection to the control unit to enable simultaneous send and receive to/from both motors. Based on this hardware setup, our custom-built image acquisition, processing, PID and motor control software achieves control cycle durations on the order of 20–30 ms corresponding to an update frequency of 33–50 Hz. Table 1 summarizes individual contributions.

We evaluate onboard performance of the solar tracker by examining the deviations between the center of the solar image and the targeted center of the spectrometer aperture. The deviations are logged during the entire campaign on board RV *Polarstern*. While such an assessment provides an estimate of the tracking precision, it does not allow for quantifying systematic tracking errors e.g. due to a misalignment of the actual and the assumed center of the spectrometer aperture. A misalignment of the latter kind leads to a systematic pointing offset i.e. the solar tracker does not point exactly to the center of the sun but slightly to the limb. Fine-tracking camera and aperture are carefully aligned in the lab to avoid such systematic errors.

Figure 2 (left) shows the logarithmic occurrence count of tracking deviations in azimuth and elevation directions. The desired tracking accuracy of $0.05°$ is red encircled. 98.7 % of the entire campaign data is within this tracking error regime. The record includes all kinds of interruptions such as shadowing by the ship's infrastructure or cloudy conditions. The tracking accuracy of the entire data accounts for $0.0076°$ (1σ), which

means, that 68.3 % of all data points feature an accuracy of this value or better. The origin of the star-shape pattern remains unclear.

Figure 2 (right) shows the dependency of the tracking precision on the angular acceleration for an illustrative day of the ship cruise. Because the PID-parameters had been changed along the entire cruise we focus on that representative day. To simplify the evaluation just the azimuth component is analyzed. The azimuth component is physically the most inert part of the system and serves as a conservative estimate. The elevation component, however, shows very similar behavior. Generally, the larger accelerations required to compensate ship movements, the poorer the tracking precision. The linear dependency of tracking precision on angular acceleration can be used to derive a maximum acceleration up to which our solar tracking performs within the required limits. If the angular acceleration does not exceed approximately $6.5° \, s^{-2}$ the tracking precision complies with the $0.05°$ requirement.

2.2 Fourier Transform Spectrometer EM27/SUN

The Bruker™ EM27/SUN FTS is a table-top Fourier Transform Spectrometer of approximately 25 kg weight. It is designed in the framework of a cooperation between KIT and Bruker™ for stationary XCO_2 and XCH_4 measurements (Gisi et al., 2012). Here, we give a brief overview of the most important features.

The EM27/SUN is constructed as a RockSolid™ pendulum interferometer with two cube corner mirrors and a CaF_2 beam splitter. The optical path difference of 1.8 cm corresponds to a spectral resolution of $0.5 \, cm^{-1}$. A 127 mm parabolic mirror together with the 0.6 mm aperture defines an semi-FOV of 2.36 mrad. With the solar disc as light source this FOV corresponds to approximately 51.0 % of the solar diameter. The InGaAs non-cooled detector (HAMAMATSU™ G12181-010K) with a sensitive area of approximately $0.8 \, mm^2$, has a spectral response from 5000 to $11\,000 \, cm^{-1}$. Typical exposure times are approximately 58 s for 10 double sided interferograms, recorded in DC-mode. Differences to the prototype device used by Gisi et al. (2012) are a slightly different focal length of 127 mm instead of 101.6 mm and a detector with a spectral

coverage of 5000 to 11 000 cm^{-1} instead of 6000 to 9000 cm^{-1}. The latter adjustment was necessary to cover the spectral range of CH$_4$ absorption. Further, a bandpass filter (Thorlabs FB1650-12, center wavenumber: 6061 cm^{-1}, FWHM: 44.0 cm^{-1}) has been mounted in front of the internal calibration lamp in order to characterize the ghost-to-parent ratio as described in Dohe et al. (2013) or Messerschmidt et al. (2010).

Gisi et al. (2012) showed, that this instrument is highly stable against thermal influences in particular as demonstrated by observations in summer and winter in Karlsruhe. Furthermore moderate mechanical stress due to deployment and dismounting do not harm the accuracy of the instrument. This makes the instrument in particular suitable for campaign purposes.

3   Data reduction and evaluation

The following section guides through the data evaluation process. Section 3.1 describes the spectral retrieval of absorber total columns from the recorded solar absorption spectra. Various quality filters (Sect. 3.2) and corrections (Sect. 3.3) guarantee that quality of the estimated XCO$_2$ and XCH$_4$ is consistently high throughout the ship cruise.

3.1   Spectral retrieval

The spectral retrieval of absorber total columns uses the software package PROFFIT v.9.6 (Hase et al., 2004). In principle, PROFFIT is capable of retrieving vertical profile information from high spectral resolution measurements of the atmospheric transmittance in direct-sun view (García et al., 2012). The medium resolution of 0.5 cm^{-1} of the EM27 FTS, however, is insufficient to extract profile information from the pressure and temperature dependent absorption line shapes. Therefore, here, a configuration is chosen that retrieves a scaling parameter for the a priori absorber profiles.

The absorber total columns to be retrieved are the ones of the targeted species CO_2 and CH_4, and the ones of the ancillary species molecular oxygen (O_2) and water vapor (H_2O). The latter is an interfering species. O_2 is used to calculate the dry air mole fraction X_{gas} of the desired target gas via

$$X_{gas} = 0.209420 \cdot \frac{C_{gas}}{C_{O_2}} \tag{1}$$

where C_{gas} is the gas total column in units $molec\,cm^{-2}$. Referencing the targeted gas abundance to the known O_2 abundance is a common approach to cancel out instrument and retrieval related errors common to the retrievals of O_2 and the target species.

The a priori profiles of CO_2 and CH_4 are taken from a CarbonTracker model run (Peters et al., 2007) for the year 2008 and from a Tracer Model 4 (TM4) run (Meirink et al., 2006) for the year 2007, respectively. Meteorological parameters such as pressure and temperature vertical profiles are based on the monthly latitudinal mean profiles provided by CIRA-86[1] (Fleming et al., 1988) that reaches up to 120 km height in 77 levels. If available, these meteorological profiles are supplemented by the daily noon-time radiosonde measurements from aboard RV *Polarstern* reaching altitudes up to 30 km height (König-Langlo, 2014). If no radiosonde data available, the data from the global model reanalysis from the National Centers for Environmental Prediction (NCEP) (Kalnay et al., 1996) is used to supplement the initial profile up to approximately 30 km height. The NCEP-data is downloaded via the Goddard auto mailer system (Schoeberl et al., 2014). This combined profile is interpolated on a 49 layer grid from measurement height up to to 120 km.

The a priori O_2 and H_2O profiles are generic profiles, that represent a typical situation.

---

[1]CIRA stands for "COSPAR International Reference Atmosphere", whereas COSPAR stands for "Committee on SPAce Research".

Title Page

Abstract	Introduction
Conclusions	References
Tables	Figures

|◄   ►|

◄   ►

Back   Close

Full Screen / Esc

Printer-friendly Version

Interactive Discussion

The calculation of atmospheric gas absorption lines are based on the HIgh resolution TRANsmission (HITRAN) database (Rothman et al., 2009) from 2008. Whereas for CH_4 the unchanged line list is used, the CO_2 line list is modified as suggested by Lamouroux et al. (2010) to take into account line-mixing effects. The line list for O_2 is
5 modified according to TCCON recommendations. Finally, the H_2O line list is based on HITRAN-updates from 2009.

Table 2 gives an overview of the most important retrieval parameters among the various spectral windows.

The Instrumental Line Shape (ILS) of the instrument is determined analyzing water
10 vapor absorption lines along a light path through ambient air in our laboratory. A 50 W light bulb is collimated and positioned at ~ 4.0 m distance to the spectrometer. A data logger (MRC, MHB-382SD) provides temperature and pressure readings to calculate the appropriate absorption line shapes. Parameters defining the ILS are retrieved together with the ambient H_2O abundance from absorption spectra in the spectral range
15 at 7000–7400 cm^{-1} using the LINEFIT software package version 14 (Hase et al., 1999). ILS retrieval parameters are 0.99594 for the modulation efficiency and 2.83×10^{-3} for the phase error in the post campaign retrieval. As long as no instrumental changes (e.g. accidental or intentional changes in the optical alignment) are undertaken, the inferred ILS parameters have been shown to be constant over month-long timescales
20 (Gisi et al., 2012; Frey et al., 2015). During the RV *Polarstern* cruise, the instrument housing had to be removed which appears to have caused a slight change of the optical alignment. To monitor and mitigate changes in the ILS, we conduct a preprocessing step which retrieves the ILS parameters from O_2 absorption lines throughout the ship cruise. Details are given in Sect. 3.3.
25 The preprocessing was performed with the python routine "Calpy_mobile" programme developed at KIT. This routine requests and downloads the meteorological profile data at the Goddard automailer system and generates the input profiles with the radiosonde data. Additionally it performs the DC-correction (Keppel-Aleks et al., 2007a)

(see Sect. 3.3) on the interferogram, the fourier transformation and finally exports it into a binary input format for PROFFIT.

3.2 Quality filters

The spectrometer was operated semi-automatically from morning to afternoon on deck
5 of the RV *Polarstern* whenever outside weather conditions were not too harsh. There-fore, spectra were recorded also under unfavorable conditions e.g. when the sun was partially obscured by ship structures or when lines-of-sight crossed the exhaust plume (EP) of the ship. To exclude such measurements from the scientific data set, we ap-ply three quality filters: The DC-filter screens strong intensity fluctuations. The O_2-filter
10 gives an estimate on the retrieval quality with the ground pressure as reference. Finally the EP-filter (Exhaust Plume) removes measurements, where the instrument´s line of sight passed the ships exhaust plume.

    The DC-filter is designed to sort out intensity fluctuations during the measurement. These fluctuations can for example be introduced by variable cirrus clouds or by the
15 ship's structures obscuring the line-of-sight. We operate the EM27/SUN FTS in the DC-mode i.e. the spectrometer records the full interferogram including its smoothly varying DC part. Strong fluctuations in the DC part are indicative for varying source brightness. Affected measurements can be corrected with the low pass filtered interferogram I_{lp} (Keppel-Aleks et al., 2007b). The implementation of the low pass is a running mean on
20 the interferogram over 61 sampling points with 5 iterations.

    However, this DC-correction removes not the entire DC-effect, and especially strong variations still appear to influence the retrieval result. Based on the DC-correction, a filter criterion DC can be defined to sort out affected measurements:

$$DC = \frac{|I_{lp}|_{max} - |I_{lp}|_{min}}{|I_{lp}|_{max}}. \tag{2}$$

25 The higher the value of the DC criterion, the stronger the effect on the retrieved trace gas. Effects of the DC filter are examined in Figs. 3 and 4 and discussed together with

the next filter. Here, we choose a filter threshold DC < 0.05 that discards 21.2 % of the recorded spectra.

The O_2-filter is based on the comparison between surface pressure calculated from the retrieved O_2 column and the in-situ measured surface pressure (König-Langlo, 2014) as suggested by Wunch et al. (2011). Deviations indicate a false measurement since the O_2 concentration in the atmosphere can be assumed constant. Taking into account a scaling factor of 0.9717 for calibrating the spectroscopically retrieved surface pressure p_{retr} to the in-situ measurements $p_{in\text{-}situ}$ (Wunch et al., 2011), the ratio

$$R_{psf} = \frac{0.9717 \times p_{retr}}{p_{in\text{-}situ}} \qquad (3)$$

scatters around unity. Here, we screen spectra whenever R_{psf} deviates by more than 0.3 % from unity removing 7.2 % of the DC-filtered spectra. To determine the filter thresholds for both the DC- and O_2-filter, we define a quality criterion Q for the retrieved XCO_2: we select a subset of representative days from 22 to 25 March. First, we remove diurnal variations from the record by fitting a 3rd order polynomial for each day and subtracting the polynomial from the retrieved XCO_2. The standard deviation of the residual XCO_2 timeseries defines our quality criterion Q in units of ppm.

Figure 3 illustrates how the DC-filter and the O_2-filter affects the quality criterion Q_{XCO_2}. In general the stricter the filter thresholds the better the precision but the fewer data passing the quality filters. Figure 4 shows the XCO_2 measurements for these four representative days and the effect of the DC- and O_2 filters with the selected thresholds. The overlap of the two filters is very little, showing that they filter for independent effects.

Under the assumption, that the 3rd order polynomial removes all geophysical variability due to local surface fluxes and advective transport, this quality criterion provides a precision estimate for the EM27/SUN amounting to $Q_{XCO_2} = 0.13$ ppm for XCO_2. Following an analogue procedure for XCH_4 yields $Q_{XCH_4} = 0.62 \times 10^{-4}$ ppb.

The third filter is the exhaust-plume filter (EP-filter). The ship's smoke pipe is located at a few ten meters distance to the spectrometer setup and rises to approximately

Full Screen / Esc

Printer-friendly Version

Interactive Discussion

12 m above deck. If the line-of-sight passes through the exhaust plume, enhancements in the observed XCO_2 are to be expected. In order to screen such observations, we calculate the enhancement pattern in the XCO_2 time series from our line-of-sight (los), the prevailing wind conditions and the ship's exhaust.

A estimated exhaust flux E_s feeds a simple plume model that calculates the XCO_2 enhancement E_{los} taking into account the relative wind speed and direction between the ship-based spectrometer and the plume. We rely on the plume diffusion model used by Bovensmann et al. (2010). Defining the x coordinate as downwind direction and the y coordinate as the crosswind direction, the enhancement E_{los} along the line-of-sight can be calculated via

$$E_{los} = \int\limits^{los} \frac{E_s}{v_{rel}} \frac{1}{\sqrt{2\pi} \cdot \sigma_y(x)} \cdot \exp\left(-\frac{1}{2} \frac{y^2}{\sigma_y(x)^2} \right) dx\, dy \tag{4}$$

where v_{rel} is the relative wind velocity between ship and plume, the parameter $\sigma_y(x) = 0.104 \cdot x^{0.894}$ dilutes the plume in crosswind direction (y). Thereby, we assume a class C for the atmospheric stability (Bovensmann et al., 2010). Here the exhaust flux $E_s := 1$ is given in arbitrary units (AU). Relative wind velocities v_{rel} and directions are taken from the records of onboard meteorological station. The line-of-sight from instrument position up to 30 m is projected into the downwind (x) and crosswind (y) direction and then, E_{los} is calculated by numerically integrating Eq. (4). Figure 5 shows a day where according to the lab book the line-of-sight passed the exhaust plume as confirmed by the record of relative wind velocities and directions. Measured O_2 columns and XCH_4 are not affected by the ship´s exhaust, XCO_2, however, is found enhanced by up to 2 ppm. Our model yields an enhancement E_{los} that is similar in temporal pattern to the observed XCO_2 enhancement confirming the overall applicability of our approach.

The EP-filter threshold is set such that whenever E_{los} is larger than 0.001 the spectrum is flagged contaminated. 11.6 % of the spectra are discarded by the EP-filter. Additionally, 2.8 % of the spectra are rejected due to contamination by the exhaust plume after inspection by eye.

In total, the three filters (DC, O$_2$ and EP) described above screen about 37.5 % of the recorded spectra.

3.3 Corrections

Three major corrections are found necessary to make the XCO$_2$ and XCH$_4$ records consistently accurate along the ship cruise: a change of the instrumental line shape (ILS) of the FTS has to be taken into account, a spurious dependency of the retrieved target gas abundances on solar zenith angle needs to be corrected, and an overall calibration factor needs to be found to make the spectroscopic measurements consistent with the WMO (World Meteorological Organization) calibration scale.

It was required to open the EM27/SUN FTS instrument housing on 18 March 2014: The instrument has the option to toggle the incoming light beam between an internal calibration lamp and the external measurement input. This switch is implemented by a movable, flat mirror, located inside the instrument's housing. The mechanics of this mirror was jammed by the additional optical filter (see Sect. 2.2), that we mounted in front of the calibration lamp. We opened the housing and removed the blocking features successfully. However, it turns out that this caused a slight change of the ILS. To cope with this change, we perform an initial test retrieval in the O$_2$ window with the ILS-modulation efficiency as a free parameter as described in Sect. 3.1. Figure 6 shows a change of about 1 % of the retrieved ILS parameter on the day when the instrument housing was opened. Here, we use the ILS determined by post-campaign measurements for spectra collected after 18 March 2014. For data collected before opening the instrument housing, we use the same post-campaign ILS but modulation efficiency reduced by 1 %. If we process the entire campaign adopting the post-campaign ILS, the difference in XCO$_2$ is approximately 0.14 and −0.10 % for XCH$_4$.

A well known (e.g. Deutscher et al., 2010; Wunch et al., 2011), spurious dependency of XCO$_2$ and XCH$_4$ retrieved from TCCON measurements on slant airmass A, defined as $A = 1/\cos(\theta)$ with solar zenith angle θ, can be reproduced by the campaign data. The higher the airmass the lower the XCO$_2$ and the XCH$_4$ retrievals. The source of this

effect remains unclear. Although uncertainties of spectroscopic line broadening parameters and shortcomings of the Voigt line shape model, are likely candidates. Wunch et al. (2011) suggest an empirical correction based on a diurnal effect combined with a θ-dependent term. Figure 7 shows that also our XCO_2 and XCH_4 retrievals clearly correlate with SZA. Given that the retrieved surface pressure derived from retrieved O_2 columns shows no such dependency, it must be driven by the CO_2 and CH_4 column retrievals. To correct for this artifact, we fit a correction polynomial $c_{SZA, gas}$ for the gases CO_2 and CH_4 according to

$$c_{SZA, gas}(\theta) = a \cdot |\theta|^3 + b \cdot |\theta| + c \tag{5}$$

where a, b, c are free fitting parameters. Thereby, the correction is by definition chosen to vanish at $\theta = 45°$ as suggested by Wunch et al. (2011) with referencing the measurement to $\theta = \pm 45°$ for forenoon and afternoon separately. The corrected XCO_2 and XCH_4 records are then calculated through

$$X_{SZA, gas} = \frac{X_{gas}(\theta)}{c_{SZA,gas}(\theta)}. \tag{6}$$

Figure 7 shows the retrieved correction parameters. For the extreme case of $\theta = 80°$ relative to $\theta = 0°$, the correction amounts to $\approx 0.6\%$ for XCO_2 and $\approx 0.4\%$ for XCH_4. A key assumption for this correction is that the measurements take place far away from localized sources and sinks of CO_2 and CH_4. So, no diurnal concentration cycles are to be expected that correlate with the assumed spurious airmass dependence. Generally, this assumption appears true for our ship-borne measurements above the Atlantic. Meteorological transport can cause advection of diurnal concentration variability from the larger source/sink region. Over the course of the entire measurement campaign, we assume that such transport effects have a statistical pattern such that the airmass correction is not contaminated in a systematic way.

Finally, we calibrate the entire campaign records to the official WMO validated TCCON station at Karlsruhe, Germany. To this end, we operate our EM27/SUN side-by-

side the Karlsruhe TCCON instrument during 4 consecutive days in May 2014 after the ship campaign. TCCON XCO_2 and XCH_4 are retrieved by the standard G-Fit v.0.4.4 software (Wunch et al., 2011). Retrievals from EM27/SUN measurements follow the approach outlined above including the quality filters described in Sect. 3.2 and the aforementioned correction terms. Hourly means $\langle X \rangle_h$ of the XCO_2 and XCH_4 are calculated and used to determine the calibration factor γ_{gas} according to

$$\gamma_{gas} = \left\langle \frac{\langle X_{EM27} \rangle_h}{\langle X_{wmo} \rangle_h} \right\rangle \tag{7}$$

where brackets indicate averaging over the entire dataset. The EM27/SUN measurements are then referenced to WMO via

$$X_{gas,wmo} = \frac{X_{gas}}{\gamma_{gas}}. \tag{8}$$

Figure 8 shows the post campaign reference measurements.

We find calibration factors $\gamma_{XCO_2} = (0.99195 \pm 0.00051)$ and $\gamma_{XCH_4} = (0.98211 \pm 0.00146)$ where the error estimate refers to the standard deviation among the calibration data set. Note that the calibration factor for O_2 (see Sect. 3.2) in the order of $\approx 2.8\%$ (≈ 0.972) is still present in the un-referenced data and is included into the calibration factor γ_{gas}.

4 XCO_2 and XCH_4 over the Atlantic

Figure 9 shows the final XCO_2 and XCH_4 records measured above the Atlantic in March/April 2014 from aboard RV *Polarstern*. All corrections (see Sect. 3.3) and quality filters (see Sect. 3.2) are applied. In order to motivate the usefulness of such ship deployments for satellite and model validation, Fig. 9 additionally shows satellite soundings from the Greenhouse Gas Observing Satellite (GOSAT) and XCO_2 and

Accurate mobile remote sensing of XCO_2 and XCH_4

F. Klappenbach et al.

XCH$_4$ modeled by the MACC-II (Monitoring Atmospheric Composition and Climate – Interim Implementation) data assimilation system (Agustí-Panareda et al., 2014; Massart et al., 2014). Satellite soundings correlated to RV *Polarstern* records with an 5° latitudinal/longitudinal radius in addition with a 4 h temporal coincidence radius (see Fig. 1). Model data is being temporally and spatially interpolated to the RV *Polarstern* measurements to avoid discontinuities.

The lower panel shows the differences of the various greenhouse gas products to the campaign record. Here averages of all EM27/SUN soundings within the coincidence criteria is subtracted from the individual satellite soundings.

For GOSAT, we discuss three different GOSAT retrieval methods, the RemoTeC-Full-Physics (FP) and RemoTeC-Proxy (Butz et al., 2011; Guerlet et al., 2013; Schepers et al., 2012) retrieval as well as the Atmospheric CO$_2$ Observations from Space (ACOS) approach (O'Dell et al., 2012; Crisp et al., 2012). Even though the in-orbit operations of GOSAT have been adapted to maximize the number of ocean-glint soundings during the campaign period, the number of coincident and quality-assured retrievals amounts to a few ten samples, largely varying among the retrieval approaches. The main difference between the RemoTeC-FP and the RemoTeC-Proxy algorithm is the way the lightpath through the atmosphere is estimated. While RemoTeC-FP retrieves aerosol parameters simultaneously with XCO$_2$ and XCH$_4$ and takes multiple scattering effects into account, the RemoTeC-Proxy approach is restricted to XCH$_4$ only and uses the retrieved CO$_2$ column together with CarbonTracker-modeled CO$_2$ as a lightpath proxy. ACOS is, as well as RemoTeC-FP, a full-physics approach i.e. simultaneously retrieving XCO$_2$ and atmospheric scattering properties. Differences between RemoTeC-FP and ACOS relate to details how aerosol and cloud scattering parameters are implemented and how the inverse problem is solved. Most importantly here, ACOS delivers many more data than RemoTeC-FP for ocean-glint soundings since RemoTeC-FP resorts to a conservative cloud and aerosol filtering scheme using the "upper edge" method (Butz et al., 2013). ACOS does not deliver XCH$_4$.

The MACC-II provides global operational analysis and forecast of CO$_2$ and CH$_4$ in near real time. Here we have used a forecast without any data assimilation with a horizontal resolution of around 80 km and 60 vertical levels from surface to 0.1 hPa. The CO$_2$ and CH$_4$ concentration fields modeled by MACC-II rely on the Integrated Forecasting System (IFS) model operated by ECMWF. The IFS has a simple carbon module (Boussetta et al., 2013) to model the CO$_2$ uptake and release from vegetation. The CO$_2$ biogenic fluxes from vegetation are adjusted to correct for large-scale biases by using a climatology of optimized CO$_2$ fluxes (Agusti-Panareda et al., 2015, ECMWF Tech Memo 2015). The CH$_4$ fluxes and other CO$_2$ fluxes are prescribed by inventories and seasonally varying climatologies, including the chemical sinks for CH$_4$ in the troposphere and stratosphere. A more detailed description of the CO$_2$ and CH$_4$ forecast configuration can be found in Agustí-Panareda et al. (2014) for CO$_2$ and in Massart et al. (2014) for CH$_4$. The plotted data stems from the "gb5b" model experiment where no assimilation is performed.

The EM27/SUN XCO$_2$ measurements from aboard RV *Polarstern*, Fig. 9 (left), show a North–South (N–S) gradient of up to 5 ppm between $\sim 45°$ N and $\sim 30°$ S at the end of the Northern Hemisphere dormant season. This is largely expected from previous assessments (e.g. Denning et al., 1995). Beside the N–S gradient, diurnal and day-to-day variations on the order of 1 ppm are found most likely originating from transport of far-away source/sink signals. Note that the exhaust of RV *Polarstern* itself is excluded from the data via the EP-filter (see Sect. 3.2).

For XCH$_4$, Fig. 9 (right), the EM27/SUN soundings find a N–S gradient of roughly 0.06 ppm between $\sim 45°$ N and $\sim 30°$ S. Diurnal and day-to-day variability on the order of 0.01 to 0.02 ppm can be observed around 30° S 35° N. Tentatively, latitudinal variability in XCH$_4$ and XCO$_2$ follows similar patterns. For example, one might speculate whether XCO$_2$ and XCH$_4$ increasing towards the Northern tropics ($\sim 10°$ N) are related to emissions of both gases from biomass burning. Though, the inner tropics lack data to confirm that hypothesis.

Full Screen / Esc

Printer-friendly Version

Interactive Discussion

Both GOSAT XCO_2 retrievals, RemoTeC-FP and ACOS, generally match the EM27/SUN observations within 2 ppm. Due to sparse data coverage, RemoTeC-FP does not allow for assessing the N–S gradient. The ACOS retrievals tentatively show a weaker N–S gradient due to XCO_2 land-nadir soundings North of 23° being somewhat lower than the ship records. Scatter of the data, however, hinders robust conclusions.

The GOSAT RemoTeC-FP and RemoTeC-Proxy XCH_4 retrievals, both agree with the ship-borne records to mostly within 0.02 ppm. As for XCO_2, the yield from RemoTeC-FP is too low to infer robust conclusions but overall RemoTeC-FP delivers XCH_4 offset by 0.01 to 0.02 ppm compared to RemoTeC-Proxy retrievals. The latter fit the validation data particularly well for the tropical ocean-glint soundings. The land-nadir soundings North of 23° N show greater differences of 0.03 to 0.04 ppm i.e. both, RemoTeC-Proxy XCH_4 and ACOS XCO_2, reveal larger differences for the Northern mid-latitude land-nadir observations than for the low-latitude ocean-glint soundings. Given that both algorithms and both species are affected, the most likely explanation is that our co-incidence criterion is too loose to assume homogeneous concentration fields in the mid-latitudes.

XCO_2, modeled by MACC-II shows excellent agreement to our ship-borne records in the Northern extratropics. Even small variations, typically introduced by transport processes, can be resolved by both, model and measurement. North of the tropics model-measurement agreement is better than 1 ppm. Differences are particularly larger in the tropics where the model overestimates XCO_2. The ship records lack data in the inner tropics due to persistent cloud cover. Largest discrepancies up to 2.0 ppm are found in the Southern Hemisphere showing a persistent underestimation. For our demonstrator study, we neglect effects due to the averaging kernel of the measurements. Such effects might be of relevance for the level of agreement found for XCO_2 in the Northern extratropics but are assumed negligible for the larger differences in the Southern Hemisphere or the inner tropics. For XCH_4, model-measurement deviations are below 0.02 ppm for most of the cases. There is no systematic underestimation in the Southern Hemisphere as it is the case for XCO_2.

However, both models increasingly overestimate the XCO_2 and XCH_4 towards the inner tropical convergence zone (ITCZ). Here, the relative deviation is larger for XCH_4 than for XCO_2, that might point to deficiencies of the assumed surface fluxes and/or the efficiency of the chemical sink for CH_4 in tropical regions.

Overall, the deployment of the EM27/SUN spectrometer on RV *Polarstern* demonstrates that the inferred latitudinal transects of XCO_2 and XCH_4 are of adequate quality to validate soundings from satellites such as GOSAT and to evaluate modeled concentration fields such as provided by the MACC-II model. The observations collected during our ∼ 5 week campaign are too sparse too allow for a statistically robust ensemble of coincidences with GOSAT but demonstrate the potential for providing satellite validation over the oceans where other validation opportunities are sparse. Already a few ship cruises, similar to the one discussed here, conducted per year would make a great asset to for XCO_2 and XCH_4 remote sensing from satellites in particular for satellites such as OCO-2 providing much denser data coverage than GOSAT. Despite the snapshot-like nature of our observations, the comparison of the ship records to the MACC-II model hints at deficiencies in the inter-hemispheric transport of the model and potentially, erroneous tropical surface fluxes for CO_2. Thereby, simultaneously comparing measured and modeled XCO_2 and XCH_4 delivers additional confidence in the conclusions since transport related errors are correlated among the two species.

5   Conclusions

The portable EM27/SUN FTS has been successfully used to record direct sunlight spectra on board the German research vessel "Polarstern". The solar tracking device could be adapted in hard- and software such that direct-sun absorption spectra could be recorded regardless of the ship's movements achieving a tracking precision better than the required 0.05° for 98.7 % of the onboard measurements. This implies that our tracking system can handle angular accelerations up to $6.5° s^{-2}$. To guarantee adequate accuracy of the retrieved XCO_2 and XCH_4 abundances, we define several

quality filters and correction steps. The data are filtered for intensity fluctuations during recording of the interferogram (DC-filter), spurious variations in the retrieved O$_2$ reference (O$_2$-filter), and XCO$_2$ retrievals contaminated by the ship's local exhaust plume (EP-filter). After quality filtering, we correct for a slight change in the ILS during the campaign, a spurious SZA dependency of the retrieved concentration records, and an overall scaling factor with respect to the WMO calibration scale. Thus, the final XCO$_2$ and XCH$_4$ concentrations are traceable to WMO standards and show an overall precision of 0.13 ppm for XCO$_2$ and 6.2 10^{-4} ppm for XCH$_4$, respectively, as estimated from the scatter of retrieved concentrations after subtracting a polynomial background.

The campaign record of XCO$_2$ and XCH$_4$ shows the expected North to South gradient overlayed by regional meteorological transport effects. The quality of our ship-based records allows for comparisons to XCO$_2$ and XCH$_4$ retrieved from GOSAT or modeled concentration fields. Although, the number of satellite coincidences is low, both the ACOS/GOSAT XCO$_2$ and RemoTeC-proxy/GOSAT XCH$_4$ tend to underestimate the interhemispheric gradient due low retrieved concentrations in the Northern extra-tropics. The comparison between the MACC-II model and the ship records shows excellent agreement for XCH$_4$ and a systematic low-biased for XCO$_2$ in the Southern Hemisphere. These comparisons recommend our setup, based on the EM27/SUN FTS and a fast solar tracker, to be used for validating models and satellites e.g. through future deployments on moving platforms such as research vessels, other ships, or land-based vehicles.

The data collected during the RV *Polarstern* cruise is public available on the PANGEA archive (PANGEA, 2014).

References

Agustí-Panareda, A., Massart, S., Chevallier, F., Boussetta, S., Balsamo, G., Beljaars, A., Ciais, P., Deutscher, N. M., Engelen, R., Jones, L., Kivi, R., Paris, J.-D., Peuch, V.-H., Sherlock, V., Vermeulen, A. T., Wennberg, P. O., and Wunch, D.: Forecasting global atmospheric CO_2, Atmos. Chem. Phys., 14, 11959–11983, doi:10.5194/acp-14-11959-2014, 2014. 7430, 7431

Bergamaschi, P., Frankenberg, C., Meirink, J. F., Krol, M., Villani, M. G., Houweling, S., Dentener, F., Dlugokencky, E. J., Miller, J. B., Gatti, L. V., Engel, A., and Levin, I.: Inverse modeling of global and regional CH_4 emissions using SCIAMACHY satellite retrievals, J. Geophys. Res.-Atmos., 114, D22301, doi:10.1029/2009JD012287, 2009. 7415

Boussetta, S., Balsamo, G., Beljaars, A., Agusti-Panareda, A., Calvet, J.-C., Jacobs, C., van den Hurk, B., Viterbo, P., Lafont, S., Dutra, E., Jarlan, L., Balzarolo, M., Papale, D., and van der Werf, G.: Natural carbon dioxide exchanges in the ECMWF integrated forecasting system: implementation and offline validation, J. Geophys Res.-Atmos., 118, 1–24, doi:10.1002/jgrd.50488, 2013. 7431

Bovensmann, H., Burrows, J., Buchwitz, M., Frerick, J., Noël, S., Rozanov, V., Chance, K., and Goede, A.: SCIAMACHY: mission objectives and measurement modes, J. Atmos. Sci., 56, 127–150, 1999. 7415

Bovensmann, H., Buchwitz, M., Burrows, J. P., Reuter, M., Krings, T., Gerilowski, K., Schneising, O., Heymann, J., Tretner, A., and Erzinger, J.: A remote sensing technique for global monitoring of power plant CO_2 emissions from space and related applications, Atmos. Meas. Tech., 3, 781–811, doi:10.5194/amt-3-781-2010, 2010. 7426

Burrows, J., Hölzle, E., Goede, A., Visser, H., and Fricke, W.: SCIAMACHY scanning imaging absorption spectrometer for atmospheric chartography, earth Observation, Acta Astronaut., 35, 445–451, doi:10.1016/0094-5765(94)00278-T, 1995. 7415

Butz, A., Guerlet, S., Hasekamp, O., Schepers, D., Galli, A., Aben, I., Frankenberg, C., Hartmann, J.-M., Tran, H., Kuze, A., Keppel-Aleks, G., Toon, G., Wunch, D., Wennberg, P., Deutscher, N., Griffith, D., Macatangay, R., Messerschmidt, J., Notholt, J., and Warneke, T.: Toward accurate CO_2 and CH_4 observations from GOSAT, Geophys. Res. Lett., 38, L14812, doi:10.1029/2011GL047888, 2011. 7430

Butz, A., Guerlet, S., Hasekamp, O. P., Kuze, A., and Suto, H.: Using ocean-glint scattered sunlight as a diagnostic tool for satellite remote sensing of greenhouse gases, Atmos. Meas. Tech., 6, 2509–2520, doi:10.5194/amt-6-2509-2013, 2013. 7430

Chevallier, F., Bréon, F.-M., and Rayner, P. J.: Contribution of the Orbiting Carbon Observatory to the estimation of CO_2 sources and sinks: theoretical study in a variational data assimilation framework, J. Geophys. Res.-Atmos., 112, D09307, doi:10.1029/2006JD007375, d09307, 2007. 7415

Chevallier, F., Ciais, P., Conway, T. J., Aalto, T., Anderson, B. E., Bousquet, P., Brunke, E. G., Ciattaglia, L., Esaki, Y., Fröhlich, M., Gomez, A., Gomez-Pelaez, A. J., Haszpra, L., Krummel, P. B., Langenfelds, R. L., Leuenberger, M., Machida, T., Maignan, F., Matsueda, H., Morguí, J. A., Mukai, H., Nakazawa, T., Peylin, P., Ramonet, M., Rivier, L., Sawa, Y., Schmidt, M., Steele, L. P., Vay, S. A., Vermeulen, A. T., Wofsy, S., and Worthy, D.: CO_2 surface fluxes at grid point scale estimated from a global 21 year reanalysis of atmospheric measurements, J. Geophys. Res.-Atmos., 115, D21307, doi:10.1029/2010JD013887, 2010. 7415

Crisp, D., Fisher, B. M., O'Dell, C., Frankenberg, C., Basilio, R., Bösch, H., Brown, L. R., Castano, R., Connor, B., Deutscher, N. M., Eldering, A., Griffith, D., Gunson, M., Kuze, A., Mandrake, L., McDuffie, J., Messerschmidt, J., Miller, C. E., Morino, I., Natraj, V., Notholt, J., O'Brien, D. M., Oyafuso, F., Polonsky, I., Robinson, J., Salawitch, R., Sherlock, V., Smyth, M., Suto, H., Taylor, T. E., Thompson, D. R., Wennberg, P. O., Wunch, D., and Yung, Y. L.: The ACOS CO_2 retrieval algorithm – Part II: Global X_{CO_2} data characterization, Atmos. Meas. Tech., 5, 687–707, doi:10.5194/amt-5-687-2012, 2012. 7430

Denning, A. S., Fung, I. Y., and Randall, D.: Latitudinal gradient of atmospheric CO_2 due to seasonal exchange with land biota, Nature, 376, 240–243, 1995. 7431

Deutscher, N. M., Griffith, D. W. T., Bryant, G. W., Wennberg, P. O., Toon, G. C., Washen-
felder, R. A., Keppel-Aleks, G., Wunch, D., Yavin, Y., Allen, N. T., Blavier, J.-F., Jiménez, R.,
Daube, B. C., Bright, A. V., Matross, D. M., Wofsy, S. C., and Park, S.: Total column CO_2
measurements at Darwin, Australia – site description and calibration against in situ aircraft
profiles, Atmos. Meas. Tech., 3, 947–958, doi:10.5194/amt-3-947-2010, 2010. 7427

Dohe, S., Sherlock, V., Hase, F., Gisi, M., Robinson, J., Sepúlveda, E., Schneider, M., and Blu-
menstock, T.: A method to correct sampling ghosts in historic near-infrared Fourier transform
spectrometer (FTS) measurements, Atmos. Meas. Tech., 6, 1981–1992, doi:10.5194/amt-6-
1981-2013, 2013. 7421

Fleming, E. L., Chandra, S., Schoeberl, M. R., and Barnett, J. J.: Monthly mean global clima-
tology of temperature, wind, geopotential height, and pressure for 0–120 km, Advances in
Space Research, 10, 3–12, doi:10.1016/0273-1177(90)90230-W, 1988. 7422

Frey, M., Hase, F., Blumenstock, T., Groß, J., Kiel, M., Mengistu Tsidu, G., Schäfer, K., Sha,
M. Kumar, and Orphal, J.: Use of portable FTIR spectrometers for detecting greenhouse
gas emissions of the megacity Berlin – Part 1: Instrumental line shape characterisation and
calibration of a quintuple of spectrometers, Atmos. Meas. Tech. Discuss., 8, 2735–2766,
doi:10.5194/amtd-8-2735-2015, 2015. 7416, 7423

García, O. E., Schneider, M., Redondas, A., González, Y., Hase, F., Blumenstock, T., and
Sepúlveda, E.: Investigating the long-term evolution of subtropical ozone profiles applying
ground-based FTIR spectrometry, Atmos. Meas. Tech., 5, 2917–2931, doi:10.5194/amt-5-
2917-2012, 2012. 7421

Geibel, M. C., Gerbig, C., and Feist, D. G.: A new fully automated FTIR system for total column
measurements of greenhouse gases, Atmos. Meas. Tech., 3, 1363–1375, doi:10.5194/amt-
3-1363-2010, 2010. 7416

Gisi, M., Hase, F., Dohe, S., and Blumenstock, T.: Camtracker: a new camera controlled
high precision solar tracker system for FTIR-spectrometers, Atmos. Meas. Tech., 4, 47–54,
doi:10.5194/amt-4-47-2011, 2011. 7417, 7418

Gisi, M., Hase, F., Dohe, S., Blumenstock, T., Simon, A., and Keens, A.: XCO_2-measurements
with a tabletop FTS using solar absorption spectroscopy, Atmos. Meas. Tech., 5, 2969–2980,
doi:10.5194/amt-5-2969-2012, 2012. 7416, 7420, 7421, 7423

Guerlet, S., Butz, A., Schepers, D., Basu, S., Hasekamp, O. P., Kuze, A., Yokota, T., Blavier, J.-
F., Deutscher, N. M., Griffith, D. W., Hase, F., Kyro, E., Morino, I., Sherlock, V., Sussmann, R.,
Galli, A., and Aben, I.: Impact of aerosol and thin cirrus on retrieving and validating XCO_2

**Accurate mobile
remote sensing of
XCO_2 and XCH_4**

F. Klappenbach et al.

Title Page

Abstract	Introduction
Conclusions	References
Tables	Figures

|◀   ▶|

◀   ▶

Back   Close

Full Screen / Esc

Printer-friendly Version

Interactive Discussion

Discussion Paper | Discussion Paper | Discussion Paper | Discussion Paper

from GOSAT shortwave infrared measurements, J. Geophys. Res.-Atmos., 118, 4887–4905, doi:10.1002/jgrd.50332, 2013. 7430

Hase, F., Blumenstock, T., and Paton-Walsh, C.: Analysis of the instrumental line shape of high-resolution Fourier transform IR spectrometers with gas cell measurements and new retrieval software, Appl. Optics, 38, 3417–3422, doi:10.1364/AO.38.003417, 1999. 7423

Hase, F., Hannigan, J., Coffey, M., Goldman, A., Höpfner, M., Jones, N., Rinsland, C., and Wood, S.: Intercomparison of retrieval codes used for the analysis of high-resolution, ground-based FTIR measurements, J. Quant. Spectrosc. Ra., 87, 25–52, doi:10.1016/j.jqsrt.2003.12.008, 2004. 7421

Kalnay, E., Kanamitsu, M., Kistler, R., Collins, W., Deaven, D., Gandin, L., Iredell, M., Saha, S., White, G., Woollen, J., Zhu, Y., Leetmaa, A., Reynolds, R., Chelliah, M., Ebisuzaki, W., Higgins, W., Janowiak, J., Mo, K. C., Ropelewski, C., Wang, J., Jenne, R., and Joseph, D.: The NCEP/NCAR 40-year reanalysis project, B. Am. Meteorol. Soc., 77, 737–471, doi:10.1175/1520-0477(1996)077%3C0437:TNYRP%3E2.0.CO;2, 1996. 7422

Kawasaki, M., Yoshioka, H., Jones, N. B., Macatangay, R., Griffith, D. W. T., Kawakami, S., Ohyama, H., Tanaka, T., Morino, I., Uchino, O., and Ibuki, T.: Usability of optical spectrum analyzer in measuring atmospheric CO_2 and CH_4 column densities: inspection with FTS and aircraft profiles in situ, Atmos. Meas. Tech., 5, 2593–2600, doi:10.5194/amt-5-2593-2012, 2012. 7416

Keppel-Aleks, G., Toon, G. C., Wennberg, P. O., and Deutscher, N. M.: Reducing the impact of source brightness fluctuations on spectra obtained by Fourier-transform spectrometry, Appl. Optics, 46, 4774–4779, doi:10.1364/AO.46.004774, 2007a. 7423

Keppel-Aleks, G., Toon, G. C., Wennberg, P. O., and Deutscher, N. M.: Reducing the impact of source brightness fluctuations on spectra obtained by Fourier-transform spectrometry, Appl. Optics, 46, 4774–4779, doi:10.1364/AO.46.004774, 2007b. 7424

Kobayashi, N., Inoue, G., Kawasaki, M., Yoshioka, H., Minomura, M., Murata, I., Nagahama, T., Matsumi, Y., Tanaka, T., Morino, I., and Ibuki, T.: Remotely operable compact instruments for measuring atmospheric CO_2 and CH_4 column densities at surface monitoring sites, Atmos. Meas. Tech., 3, 1103–1112, doi:10.5194/amt-3-1103-2010, 2010. 7416

König-Langlo, G.: Radiosonde During POLARSTERN Cruise PS83 (ANT-XXIX/10), Bremerhaven, Germany, doi:10.1594/PANGAEA.832783, 2014. 7422, 7425

Krings, T., Gerilowski, K., Buchwitz, M., Reuter, M., Tretner, A., Erzinger, J., Heinze, D., Pflüger, U., Burrows, J. P., and Bovensmann, H.: MAMAP – a new spectrometer system

for column-averaged methane and carbon dioxide observations from aircraft: retrieval algorithm and first inversions for point source emission rates, Atmos. Meas. Tech., 4, 1735–1758, doi:10.5194/amt-4-1735-2011, 2011. 7416

Lamouroux, J., Tran, H., Laraia, A., Gamache, R., Rothman, L., Gordon, I., and Hartmann, J.-M.: Updated database plus software for line-mixing in CO_2 infrared spectra and their test using laboratory spectra in the 1.5–2.3 µm region, J. Quant. Spectrosc. Ra., 111, 2321–2331, doi:10.1016/j.jqsrt.2010.03.006, XVIth Symposium on High Resolution Molecular Spectroscopy (HighRus-2009) XVIth Symposium on High Resolution Molecular Spectroscopy, 2010. 7423, 7443

Masarie, K. A., Peters, W., Jacobson, A. R., and Tans, P. P.: ObsPack: a framework for the preparation, delivery, and attribution of atmospheric greenhouse gas measurements, Earth Syst. Sci. Data, 6, 375–384, doi:10.5194/essd-6-375-2014, 2014. 7415

Massart, S., Agusti-Panareda, A., Aben, I., Butz, A., Chevallier, F., Crevoisier, C., Engelen, R., Frankenberg, C., and Hasekamp, O.: Assimilation of atmospheric methane products into the MACC-II system: from SCIAMACHY to TANSO and IASI, Atmos. Chem. Phys., 14, 6139–6158, doi:10.5194/acp-14-6139-2014, 2014. 7430, 7431

Meirink, J. F., Eskes, H. J., and Goede, A. P. H.: Sensitivity analysis of methane emissions derived from SCIAMACHY observations through inverse modelling, Atmos. Chem. Phys., 6, 1275–1292, doi:10.5194/acp-6-1275-2006, 2006. 7422

Messerschmidt, J., Machatangay, R., Notholt, J., Petri, C., Warneke, T., and Weinzierl, C.: Side by side measurements of CO_2 by ground-based Fourier transform spectrometry (FTS), Tellus B, 62, 749–758, doi:10.1111/j.1600-0889.2010.00491.x, 2010. 7421

Notholt, J., Beninga, I., and Schrems, O.: Shipborne FT-IR Measurements of Atmospheric Trace Gases on a South (33° S) to North (53° N) Atlantic Traverse, Appl. Spectrosc., 49, 1525–1527, 1995. 7416

O'Dell, C. W., Connor, B., Bösch, H., O'Brien, D., Frankenberg, C., Castano, R., Christi, M., Eldering, D., Fisher, B., Gunson, M., McDuffie, J., Miller, C. E., Natraj, V., Oyafuso, F., Polonsky, I., Smyth, M., Taylor, T., Toon, G. C., Wennberg, P. O., and Wunch, D.: The ACOS CO_2 retrieval algorithm – Part 1: Description and validation against synthetic observations, Atmos. Meas. Tech., 5, 99–121, doi:10.5194/amt-5-99-2012, 2012. 7430

PANGEA: XCO_2 and XCH_4 Total Column Measurement ANT XXIX/10 North–South Gradient, PANGEA, Bremerhaven, Germany, doi:10.1594/PANGAEA.843880, 2014. 7434

Title Page

Abstract | Introduction

Conclusions | References

Tables | Figures

|◄ | ►|

◄ | ►

Back | Close

Full Screen / Esc

Printer-friendly Version

Interactive Discussion

Peters, W., Jacobson, A. R., Sweeney, C., Andrews, A. E., Conway, T. J., Masarie, K., Miller, J. B., Bruhwiler, L. M. P., Pétron, G., Hirsch, A. I., Worthy, D. E. J., van der Werf, G. R., Randerson, J. T., Wennberg, P. O., Krol, M. C., and Tans, P. P.: An atmospheric perspective on North American carbon dioxide exchange: CarbonTracker, P. Natl. Acad. Sci. USA, 104, 18925–18930, doi:10.1073/pnas.0708986104, 2007. 7422

Petri, C., Warneke, T., Jones, N., Ridder, T., Messerschmidt, J., Weinzierl, T., Geibel, M., and Notholt, J.: Remote sensing of CO_2 and CH_4 using solar absorption spectrometry with a low resolution spectrometer, Atmos. Meas. Tech., 5, 1627–1635, doi:10.5194/amt-5-1627-2012, 2012. 7416

Peylin, P., Law, R. M., Gurney, K. R., Chevallier, F., Jacobson, A. R., Maki, T., Niwa, Y., Patra, P. K., Peters, W., Rayner, P. J., Rödenbeck, C., van der Laan-Luijkx, I. T., and Zhang, X.: Global atmospheric carbon budget: results from an ensemble of atmospheric CO_2 inversions, Biogeosciences, 10, 6699–6720, doi:10.5194/bg-10-6699-2013, 2013. 7415

Rayner, P. J. and O'Brien, D. M.: The utility of remotely sensed CO_2 concentration data in surface source inversions, Geophys. Res. Lett., 28, 175–178, doi:10.1029/2000GL011912, 2001. 7415

Rothman, L., Gordon, I., Barbe, A., Benner, D., Bernath, P., Birk, M., Boudon, V., Brown, L., Campargue, A., Champion, J.-P., Chance, K., Coudert, L., Dana, V., Devi, V., Fally, S., Flaud, J.-M., Gamache, R., Goldman, A., Jacquemart, D., Kleiner, I., Lacome, N., Lafferty, W., Mandin, J.-Y., Massie, S., Mikhailenko, S., Miller, C., Moazzen-Ahmadi, N., Naumenko, O., Nikitin, A., Orphal, J., Perevalov, V., Perrin, A., Predoi-Cross, A., Rinsland, C., Rotger, M., Ŝimecková, M., Smith, M., Sung, K., Tashkun, S., Tennyson, J., Toth, R., Vandaele, A., and Auwera, J. V.: The HITRAN 2008 molecular spectroscopic database, J. Quant. Spectrosc. Ra., 110, 533–572, doi:10.1016/j.jqsrt.2009.02.013, 2009. 7423

Schepers, D., Guerlet, S., Butz, A., Landgraf, J., Frankenberg, C., Hasekamp, O., Blavier, J.-F., Deutscher, N. M., Griffith, D. W. T., Hase, F., Kyro, E., Morino, I., Sherlock, V., Sussmann, R., and Aben, I.: Methane retrievals from Greenhouse Gases Observing Satellite (GOSAT) shortwave infrared measurements: performance comparison of proxy and physics retrieval algorithms, J. Geophys. Res.-Atmos., 117, D10307, doi:10.1029/2012JD017549, 2012. 7430

Schneider, M., Cuevas, E., Hernández, E. S., Hase, F., Blumenstock, T., García, J. C. G., and Ángel J. Gómez Peláez: Total Carbon Column Observing Network (TCCON) activities at

Izaña, Tenerife, Optica pura y aplicada, 1–4, available at: http://dialnet.unirioja.es/servlet/articulo?codigo=3867004 (last access: 17 July 2015), 2012. 7416

Schoeberl, M. R., Newman, P. A., and Lait, L. R.: Gridded meeorological data (analysis) from NMC:GG1X1:E01:SSIAVN, available at: http://acdb-ext.gsfc.nasa.gov/Data_services/automailer/ (last access: 17 July 2015), 2014. 7422

Stocker, T. F., Dahe, Q., and Plattner, G.-K.: Climate Change 2013: The Physical Science Basis, Working Group I Contribution to the Fifth Assessment Report of the Intergovernmental Panel on Climate Change, Summary for Policymakers (IPCC, 2013), Cambridge University Press, Cambridge, UK and New York, NY, USA, 2013. 7415

TCCON-Wiki: TCCON-Wiki, available at: https://tccon-wiki.caltech.edu/ (last access: 17 July 2015), 2015. 7415

Warneke, T., de Beek, R., Buchwitz, M., Notholt, J., Schulz, A., Velazco, V., and Schrems, O.: Shipborne solar absorption measurements of CO_2, CH_4, N_2O and CO and comparison with SCIAMACHY WFM-DOAS retrievals, Atmos. Chem. Phys., 5, 2029–2034, doi:10.5194/acp-5-2029-2005, 2005. 7416

Wunch, D., Toon, G. C., Wennberg, P. O., Wofsy, S. C., Stephens, B. B., Fischer, M. L., Uchino, O., Abshire, J. B., Bernath, P., Biraud, S. C., Blavier, J.-F. L., Boone, C., Bowman, K. P., Browell, E. V., Campos, T., Connor, B. J., Daube, B. C., Deutscher, N. M., Diao, M., Elkins, J. W., Gerbig, C., Gottlieb, E., Griffith, D. W. T., Hurst, D. F., Jiménez, R., Keppel-Aleks, G., Kort, E. A., Macatangay, R., Machida, T., Matsueda, H., Moore, F., Morino, I., Park, S., Robinson, J., Roehl, C. M., Sawa, Y., Sherlock, V., Sweeney, C., Tanaka, T., and Zondlo, M. A.: Calibration of the Total Carbon Column Observing Network using aircraft profile data, Atmos. Meas. Tech., 3, 1351–1362, doi:10.5194/amt-3-1351-2010, 2010. 7415

Wunch, D., Toon, G., Blavier, J., Waschenfelder, R., Notholt, J., Connor, B., Griffith, D., and SherlockSherlock, V.: The Total Carbon Column Observing Network, Philos. T. Roy. Soc. A, 369, 2087–2112, 2011, doi:10.1098/rsta.2010.0240, 2011. 7415, 7425, 7427, 7428, 7429, 7443

Title Page

Abstract | Introduction

Conclusions | References

Tables | Figures

|◄ | ►|

◄ | ►

Back | Close

Full Screen / Esc

Printer-friendly Version

Interactive Discussion

Table 1. Leading contributions to the duration of fine-tracking control cycles of the solar tracker (average values retrieved from housekeeping data logged during the measurement campaign aboard RV *Polarstern*).

Task	Duration ms
Image acquisition	≈ 10
Image processing	< 3
Motor position request	5–10
Update motor speed	5–10
Overall average	≈ 22

Table 2. List of key retrieval parameters. The line lists are altered from the original HITRAN line lists where "mod" indicates a modification suggested by Lamouroux et al. (2010) to take line mixing effects into account. Likewise "TCCON" indicates a modification suggested by Wunch et al. (2011).

	CO_2	CH_4	O_2	H_2O
spectral window cm^{-1}	6173–6390	5897–6145	7765–8005	8353.4–8463.1
line list	HITRAN08 (mod)	HITRAN08	HITRAN08 (TCCON)	HITRAN09 (TCCON)
disturbing gas	H_2O, CH_4	H_2O, CO_2	H_2O	–
continuum points	40	20	25	5
sza dependency ($\Theta = 80°$)	$\approx 0.6\%$	$\approx 0.4\%$	none	not assessed
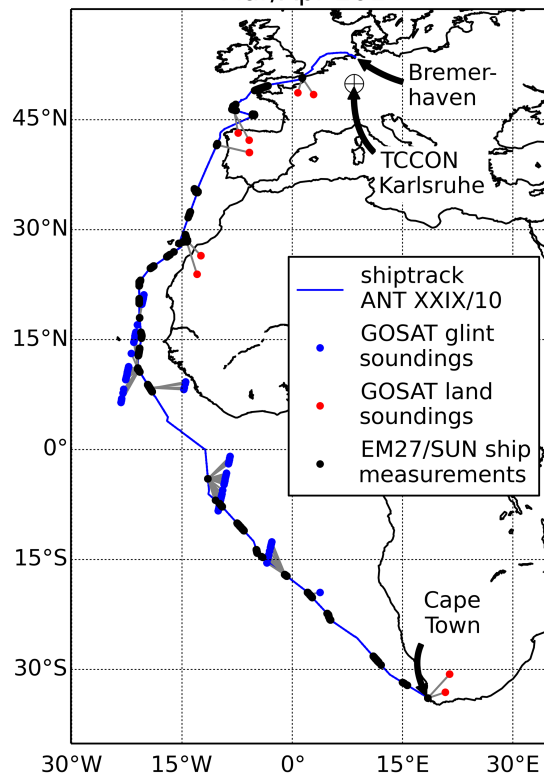
Figure 1. The ship track of the ANT XXIX/10 RV *Polarstern* cruise (blue line). Valid data is marked black. GOSAT-soundings that coincide with ship based measurements within ±4 h and 5° (lat, lon) are marked in blue (ocean) and red (land) and interconnected (gray lines).
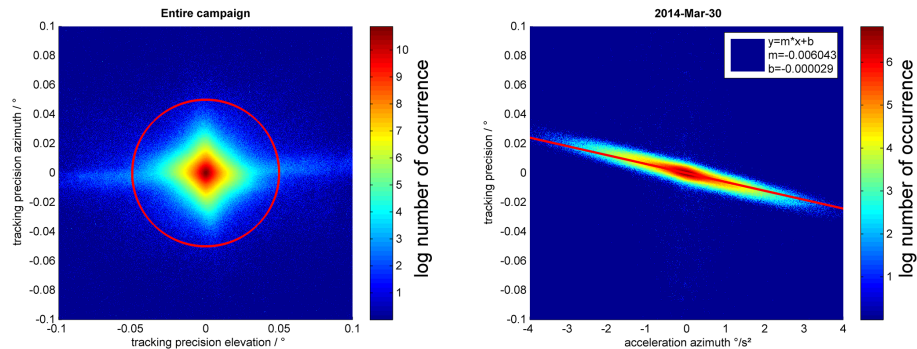
Figure 2. Both figures show occurrence of tracking errors in logarithmic color code. The left figure counts azimuth and elevation tracking errors for the entire campaign record. The red circle defines the desired 0.05° tracking precision. 98.7 % of the data points are within the circle. The right figure shows azimuth tracking precision vs. angular azimuthal acceleration for a representative day with significant angular accelerations due to a rougher sea than other days.
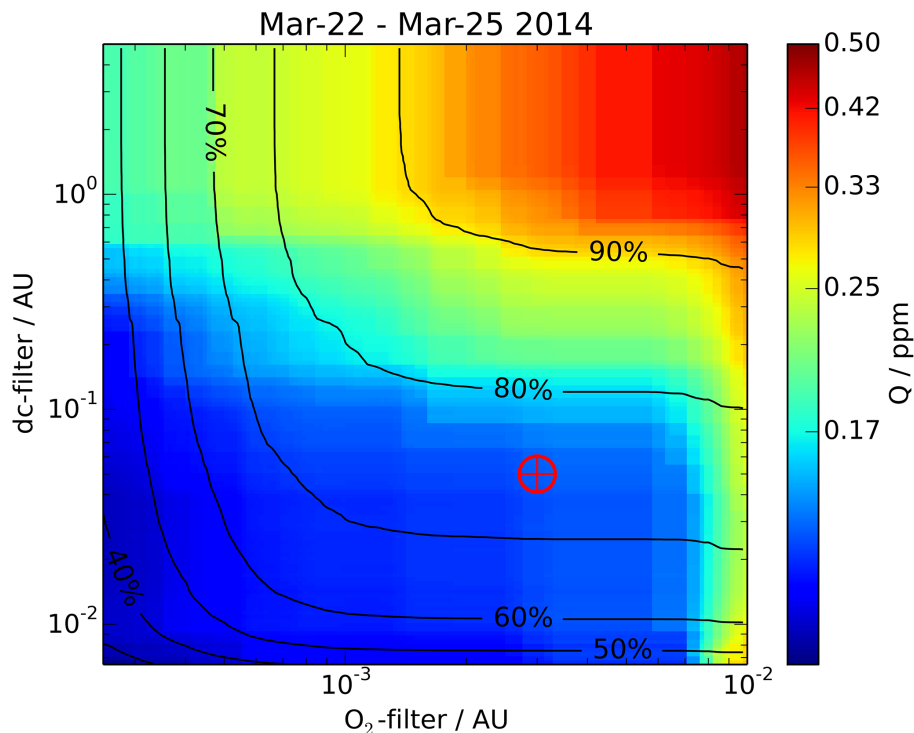
Figure 3. Effect of filter threshold for the O$_2$-filter (abscissa) and the DC-filter (ordinate) on the standard deviation of retrieved XCO$_2$ (color coded in logarithmic scale). Standard deviation of XCO$_2$ is calculated for four sample days after subtracting a 3rd order polynomial that accounts for diurnal and day-to-day variability. The data yield is overlayed as solid black contours. The finally chosen filter thresholds (5 % for the DC-filter and 0.3 % for the O$_2$-filter) are marked with the red marker.
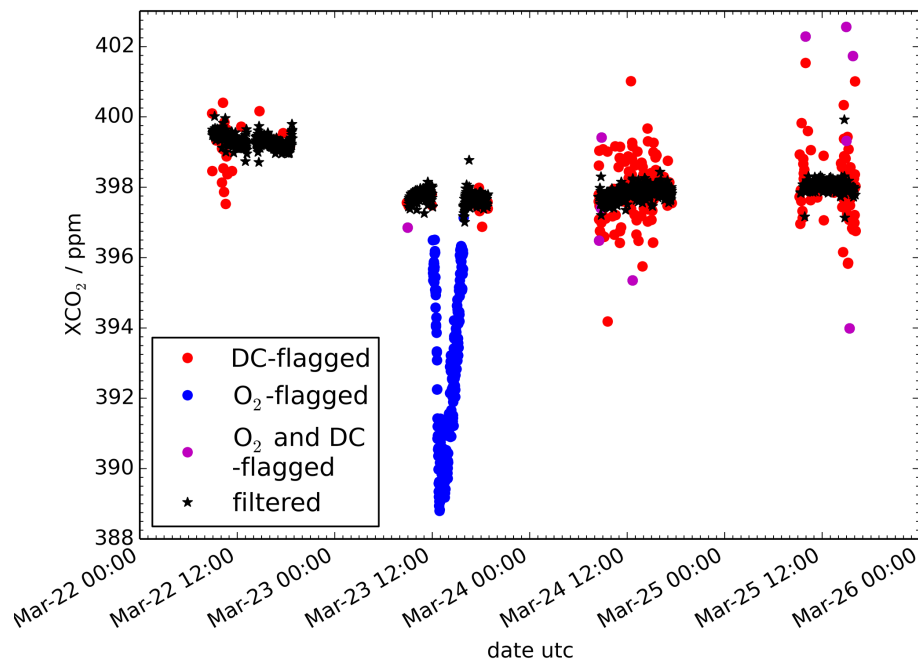
Figure 4. Effect of the DC-filter and the O$_2$-filter on the retrieved XCO$_2$ for four sample days during the campaign. The outlier on 23 March that is caught by the O$_2$-filter originates from a malfunction of the sun-tracker that caused instable pointing. The days after were affected by small but opaque clouds that disturbed some measurements which is caught by the DC-filter.
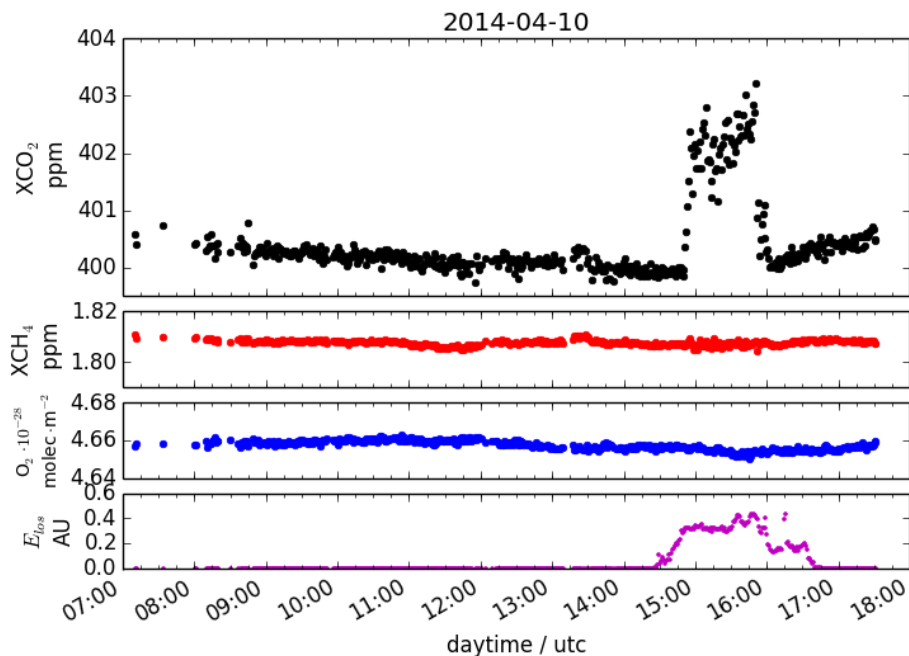
Figure 5. XCO$_2$ (top) record for a representative day after applying the DC and O$_2$ quality filters. The XCH$_4$ (upper middle, red) and O$_2$ (lower middle, blue) retrievals indicate no enhancements. In contrast, the XCO$_2$ enhancement of more than 2 ppm between 3–5 p.m. can be related to the lines-of-sight crossing the ship's exhaust plume. The calculated enhancement E_{los} (bottom) drives the EP-filter with a rejection threshold set at 0.001.
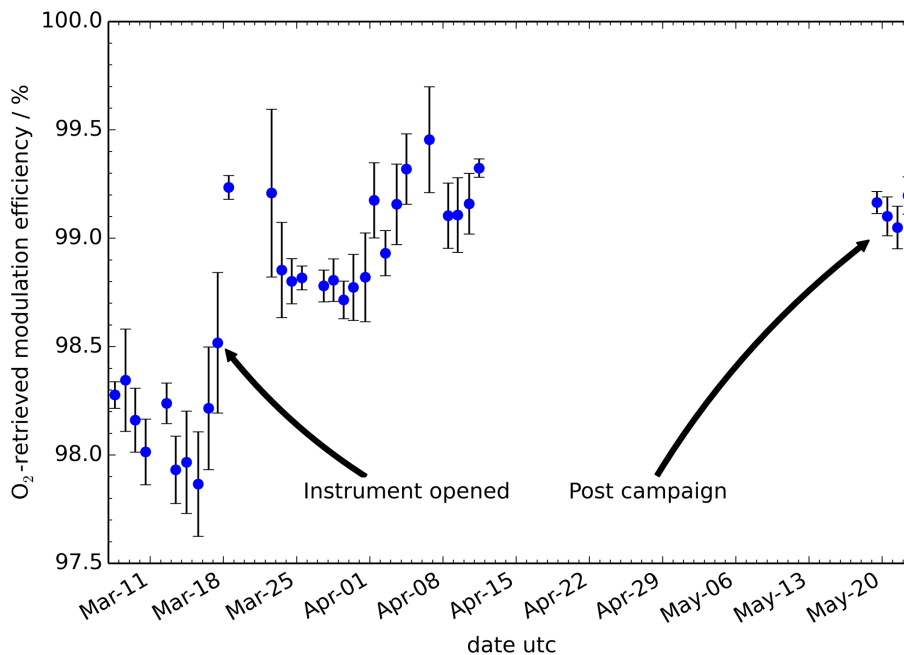
Figure 6. Daily averages of the modulation efficiency driving the adopted ILS retrieved from O_2 absorption lines during the campaign. A sudden step of 1 % can be observed after the instrument housing was opened on 18 March 2014.
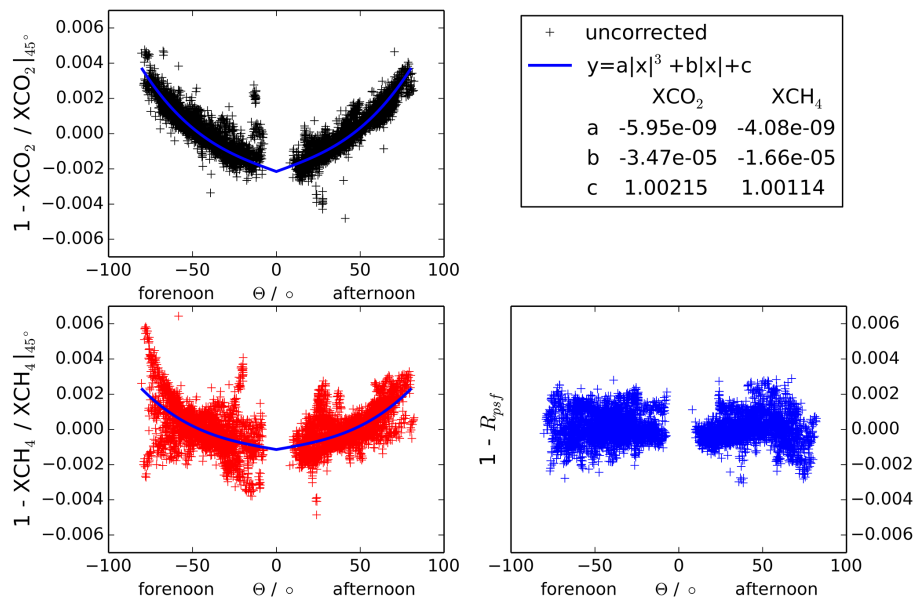
Figure 7. SZA dependency for CO_2 (upper left, referenced to XCO_2 at forenoon/afternoon SZA = 45°), CH_4 (lower left, referenced to XCH_4 at forenoon/afternoon SZA = 45°), and O_2 (lower right, surface pressure referenced O_2 retrieval R_{psf} s. Eq. (3) as a function of SZA θ. Solid lines show the fitted SZA correction function.
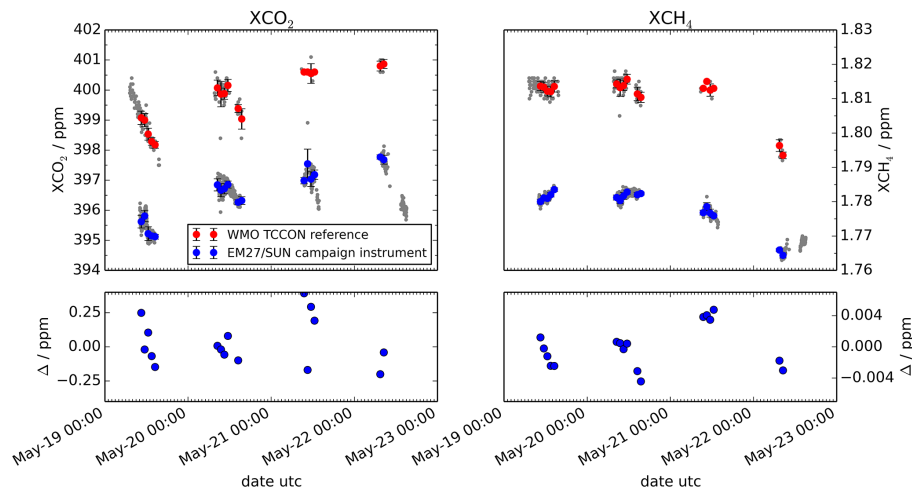
Figure 8. Post campaign measurements in Karlsruhe are used to retrieve the WMO-calibration factor for each gas. Hourly averages are taken for the TCCON reference (red) and the EM27/SUN measurements (blue). The calibration residual (lower panel) is defined as $\Delta :=$ $\langle X_{wmo} \rangle_h - \langle X_{gas,wmo} \rangle_h$.

Title Page

Abstract | Introduction

Conclusions | References

Tables | Figures
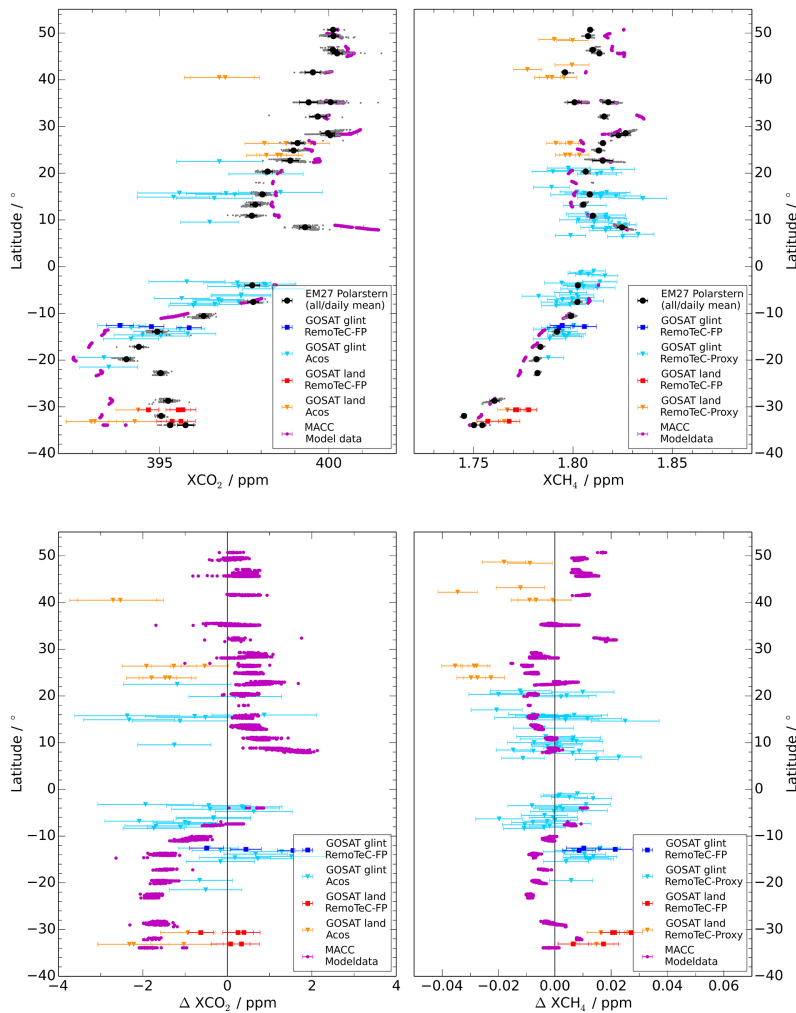
|◄ | ►|

◄ | ►

Back | Close

Full Screen / Esc

Printer-friendly Version

Interactive Discussion

Figure 9. Latitudinal transects of XCO_2 (left) and XCH_4 (right) for the ship-borne EM27/SUN measurements (daily averages black dots, all data gray dots) and various correlative data sets (top) as well as differences of the latter to our ship records (bottom). For XCO_2, correlative datasets are the RemoTeC-FP retrievals from GOSAT (ocean-glint blue, land-nadir red), the ACOS retrievals from GOSAT (ocean-glint light blue, land-nadir orange), and XCO_2 modeled by the MACC-II model (purple). For XCH_4, correlative datasets are the RemoTeC-FP retrievals from GOSAT (ocean-glint blue, land-nadir red), the RemoTeC-Proxy retrievals from GOSAT (ocean-glint light blue, land-nadir orange), and XCH_4 modeled by the MACC-II model (purple). For GOSAT, soundings are coincident whenever they are conducted within 5° latitude/longitude of the ship track and within a ±4h time frame. XCO_2 and XCH_4 differences shown in the lower panels are calculated according to $\Delta = X - \langle X_{EM27} \rangle_{4\,h}$ where the brackets indicate averaging over 4 h.

Title Page

Abstract | Introduction

Conclusions | References

Tables | Figures

|◄ | ►|

◄ | ►

Back | Close

Full Screen / Esc

Printer-friendly Version

Interactive Discussion